

PAPER

SOLPS analysis of the MAST-U divertor with the effect of heating power and pumping on the access to detachment in the Super-x configuration

To cite this article: E Havlíková *et al* 2015 *Plasma Phys. Control. Fusion* **57** 115001

View the [article online](#) for updates and enhancements.

Related content

- [Investigation of conventional and Super-X divertor configurations of MAST Upgrade using scrape-off layer plasma simulation](#)
E Havlíková, W Fundamenski, M Wischmeier *et al*.
- [Benchmarking of a 1D scrape-off layer code SOLF1D with SOLPS and its use in modelling long-legged divertors](#)
E Havlíková, W Fundamenski, F Subba *et al*.
- [Assessment of SOLPS5.0 divertor solutions with drifts and currents against L-mode experiments in ASDEX Upgrade and JET](#)
L Aho-Mantila, S Potzel, D P Coster *et al*.

Recent citations

- [Experimental simulation of the Super-X divertor for detached plasma using TPD-Sheet IV](#)
Toshikio Takimoto *et al*
- [Proposal of an alternative upper divertor in ASDEX Upgrade supported by EMC3-EIRENE simulations](#)
T. Lunt *et al*
- [Using SOLPS to confirm the importance of total flux expansion in Super-X divertors](#)
D Moulton *et al*

SOLPS analysis of the MAST-U divertor with the effect of heating power and pumping on the access to detachment in the Super-x configuration

E Havlíčková¹, J Harrison¹, B Lipschultz², G Fishpool¹, A Kirk¹,
A Thornton¹, M Wischmeier³, S Elmore¹ and S Allan¹

¹ Culham Centre for Fusion Energy, Culham Science Centre, Abingdon, OX14 3DB, UK

² Department of Physics, University of York, Heslington, York, YO10 5DD, UK

³ Max-Planck Institut für Plasmaphysik, Boltzmannstraße 2, D-85748 Garching, Germany

E-mail: eva.havlickova@ccfe.ac.uk

Received 20 May 2015

Accepted for publication 2 July 2015

Published 26 August 2015



Abstract

SOLPS simulations of MAST-U have been carried out to identify in more detail the physics and operational properties of novel divertor configurations such as Super-x divertor (SXD), in particular the physics of detachment. A well diagnosed L-mode discharge from MAST has been utilised to determine L-mode transport coefficients representative for MAST-U L-mode plasmas. Simulations show that under the same core plasma conditions, the MAST-U SXD is strongly detached whilst the conventional divertor (CD) is not (1 eV versus 20 eV at the divertor plate). The detachment and higher power losses (1.6×) in the SXD versus the attached CD lead to a factor of 25 reduction in the target power load and are attributed to changes in radial location of the target. An attached regime can be established for the SXD in L-mode for higher pumping speed and/or heating power. In contrast, the simulation predicts that the MAST-U CD requires 3× higher density or 4× reduced power than the SXD to detach. Comparing two versions of the SXD, each with a different amount of poloidal expansion in the region near the divertor plate, we find that the effect of additional poloidal flux expansion of the SXD on an already detached plasma is small for a change in flux expansion in volume by a factor of 2–3 (target temperature 0.7 eV versus 1.1 eV). The poloidal flux expansion re-arranges the radiation pattern with only a small increase in divertor power losses (1.06×) compared to changing from the CD to SXD topology. By artificially increasing the leakage from the divertor chamber, we confirmed that the tight closure of the divertor region leads to strong increases in neutral density with concomitant power losses.

Keywords: MAST Upgrade, Super-X divertor, detachment

(Some figures may appear in colour only in the online journal)

1. Introduction

The MAST-U experiment [1, 2] with its flexible divertor geometry will provide an opportunity to contribute to power exhaust physics in issues such as detachment or power handling which constitutes one of the most important problems for operation of DEMO-sized devices. The new divertor design

in MAST-U enables the so-called Super-x divertor (SXD) [3] where the target power load is reduced, and detachment achieved, compared to a conventional divertor (CD). This is due to the combined effect of increased connection length, larger flux expansion and larger target radius [4] as well as larger volumetric power losses [3, 5]. The device will be also equipped with a new central column allowing for increased

plasma current, pulse duration and toroidal field compared to MAST.

A modelling activity has been undertaken using SOLPS5.0 [6] with kinetic treatment of neutrals (EIRENE) to predict divertor conditions in MAST-U where two key divertor features are—(i) flexible magnetic topology in the divertor and (ii) improved divertor closure by baffling. Three magnetic configurations of MAST-U are considered—(i) a conventional divertor with small target radius and small flux expansion, (ii) a Super-x divertor with large target radius and large poloidal flux expansion (SXD1), (iii) a Super-x divertor with large target radius, but small poloidal flux expansion (SXD2). To decouple the effect of magnetic topology and neutral plugging in the divertor, an SXD divertor with the baffle removed is also analyzed (SXD3). The effect of the SXD on plasma parameters in both attached and detached conditions has been investigated by modelling in recent publications [7, 8], and high radiation cases with impurity seeding have been analyzed in [9, 10]. SOLPS was also used in MAST-U design studies [2] to optimize the baffle position using modelling results with different cross-field transport assumptions. In this paper, predictions for MAST-U are made for the first time using simulation parameters derived directly from a benchmarking of the code against MAST experiment. For this purpose, a typical L-mode discharge has been utilised to obtain representative radial transport coefficients. A similar technique is used in [11, 12] in different collisionality regimes including detached cases. The physics of SOLPS5.0 and the equations used in the code are described in [6].

The magnetic topology of the divertor affects its operational regime and the access to detachment. Although attached plasmas are ultimately undesirable, the transition from attached conditions to detachment allows us to study the critical detachment process. Current MAST discharges are low in divertor power and temperature and it is expected that such conditions would lead to a detached plasma in MAST-U with the SXD. MAST-U will be, however, equipped with a system of cryopumps and a new NBI heating system. Pumping speed and input power scans are therefore performed to estimate the operating window where we would expect attached divertor conditions. Note that results presented in the paper are obtained for a representative L-mode case at constant density and radial transport, and therefore do not cover the whole operational space of MAST-U, especially H-mode plasmas. In addition, this study is representative of steady-state conditions and omits for example that passive pumping on the main chamber walls is likely to allow attached operation earlier in the discharge before the neutral pressure in the divertor chamber builds up.

2. MAST L-mode experiment as described by SOL transport modelling

2.1. MAST experiment and simulation parameters

An NBI heated connected double-null MAST discharge 30356 has been selected as a test case for a comparison with SOLPS and for an extrapolation to MAST-U in section 3.

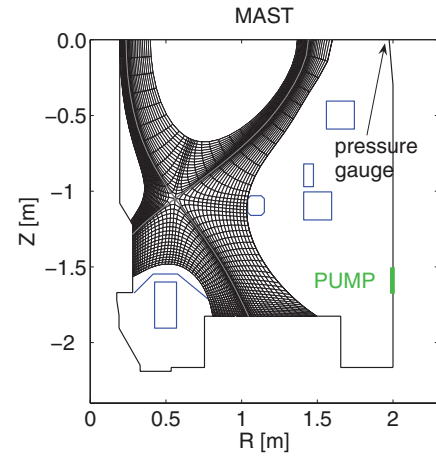


Figure 1. Simulation grid for the MAST discharge 30356. The position of the pump in the simulation and the position of the pressure gauge in the experiment are indicated.

Available diagnostics for this shot include Thomson scattering (TS), divertor Langmuir probes (LP) and infrared thermography (IR). Experimental data are taken in a quiescent period at 240 ms with the plasma current of 750 kA.

A simulation grid is shown in figure 1. The input power to the grid (the power crossing the core boundary) is assumed to be $P_{\text{inp}} = 1.7$ MW, which is derived as $P_{\text{inp}} \approx P_{\text{heat}} - P_{\text{rad}} - dW/dt$ where P_{heat} is the heating power, P_{rad} is the radiated power measured by bolometry and dW/dt (often large in MAST) is the rate of change of the stored magnetic energy from EFIT. P_{inp} is also estimated from IR measurements to reduce a possible error. For this discharge, the power arriving to the targets measured by IR is approximately 1.1 MW taking into account the wetted fraction of the divertor of 0.78. This also leads to $P_{\text{inp}} \approx 1.7$ MW if 35% power loss (as predicted by SOLPS) is assumed in the scrape-off layer (SOL). Therefore, the estimate from the expression above is consistent with the IR data for this discharge.

At the simulated time, the gas fuelling was turning off and there was around 6.5×10^{21} atoms s^{-1} of gas fuelling from the high field side. The source of neutrals from NBI in MAST is normally small compared with gas fuelling from the gas valves or recycling, approximately 4.5×10^{20} atoms s^{-1} . In the code, the fuelling is simulated as a source from the core and its strength is adjusted to match the density at the core boundary $n_{\text{core}} = 1.3 \times 10^{19} \text{ m}^{-3}$ prescribed by the experimental profile from TS. The separatrix density in the simulation is approximately $0.7 \times 10^{19} \text{ m}^{-3}$. The pump in MAST is located in the lower part of the chamber (indicated in figure 1). The pumping speed is a free model parameter and in the simulation, we assume the pumping speed of $10.7 \text{ m}^3 \text{ s}^{-1}$ as it was calculated in [13]. Beside the pump, there is no pumping in the model on the main chamber walls or targets where the recycling coefficient is set to $R = 1$.

Radial transport coefficients in this MAST case are chosen to fit the experimental profiles of n_e and T_e from TS and are assumed to be poloidally uniform (see [14] for other discharges). The radial particle diffusivity is $4 \text{ m}^2 \text{ s}^{-1}$ everywhere and the radial heat conductivity for both electron and ions is $10 \text{ m}^2 \text{ s}^{-1}$ inside the separatrix and $4 \text{ m}^2 \text{ s}^{-1}$ outside

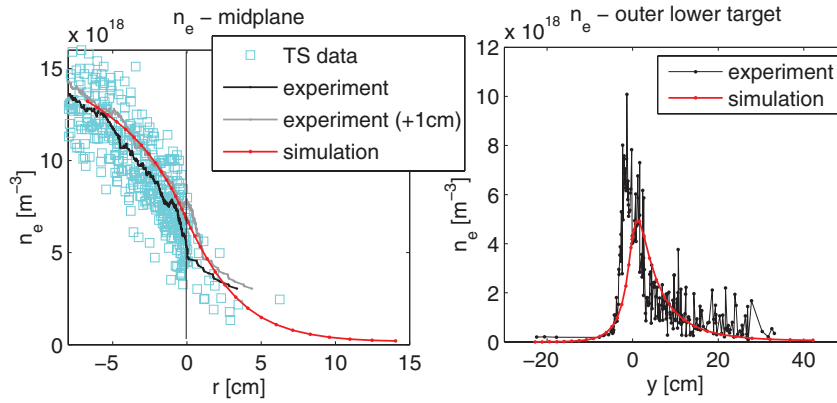


Figure 2. Radial profiles of the electron density from the experiment and simulation at the outer midplane (left) and at the outer target (right).

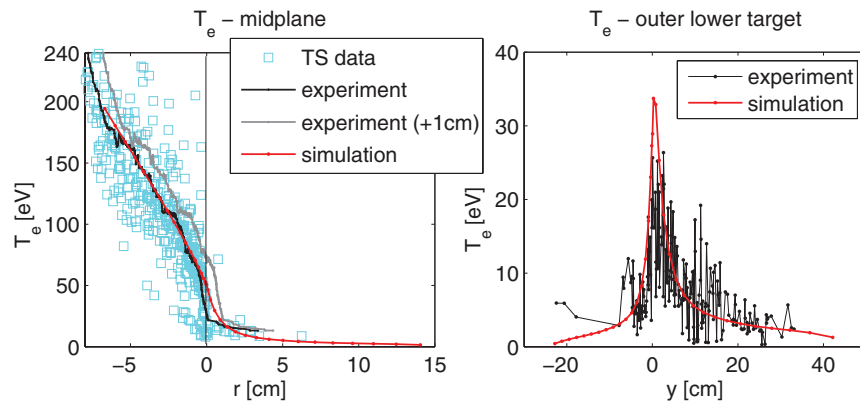


Figure 3. Radial profiles of the electron temperature from the experiment and simulation at the outer midplane (left) and at the outer target (right).

the separatrix. It appears that L-mode discharges such as 30356 require relatively large radial heat diffusivity χ_1 in the simulation inside the separatrix to reproduce experimentally observed slope in the temperature profiles. Large heat diffusivities in the edge region of the core are also obtained from transport analysis in TRANSP simulations [15].

Additional assumptions used in the simulation include: the carbon chemical sputtering coefficient of 3% (the simulation includes both chemical and physical sputtering from the walls and targets), the heat flux limiters of 0.3 and 1.0 for electron and ions, the viscous ion flux limiter of 0.5 (this corresponds to a moderate limiting typically used in SOL simulations, the limiters are defined in [6]). The sensitivity of results to the choice of the pumping speed, the chemical sputtering coefficient and the flux limiters is discussed in the appendix A. The simulation shows a large effect of the ion heat flux limiter, while the effect of the electron heat flux and the viscous flux limiters is less significant. The ion heat flux limiter modifies both upstream and target ion temperature and its choice is important if a comparison with T_i measurement is concerned. Finally, a simulation without drifts and neutral–neutral collisions is considered.

2.2. Comparison of simulation results and experimental data

Experimental profiles of the density and temperature at the outer midplane are obtained by averaging TS profiles to

remove scatter in the raw data. The profiles are shown in figures 2 and 3 on the left (black) with the raw TS data (cyan) and are overlaid by simulation results (red). On the right, target profiles from LP are shown. The experimental profiles at the midplane are also shown shifted by 1 cm with respect to the original position to take into account an uncertainty in the separatrix location, hence the separatrix density and temperature. Eventually, this uncertainty can be used to match the target parameters better, and typically, a 1 cm error is allowed based on the accuracy of the equilibrium reconstruction. Further to this, see our comment in the appendix A. Figures 2 and 3 show reasonable agreement between SOLPS and the experiment within errors in the measured data, the separatrix location and uncertainties in simulation parameters.

The simulated energy flux density at the target compares very well with the IR measurement (figure 4 left) for the given P_{inp} and χ_1 and the IR data is in good agreement with the LP data (figure 4 right). The energy flux density from IR was derived from the divertor surface temperature using the THEODOR code with a surface layer [16]. Note that both the LP and IR measurements are symmetric between the lower and upper divertors in this double-null discharge, therefore only the data from the lower divertor are used for comparison. The simulated λ_Q calculated as $\lambda_Q = \int Q_t dy / Q_t^{\text{max}}$ and mapped to the midplane is 1.7 cm and can be compared with other MAST discharges in [17]. The integral width obtained from

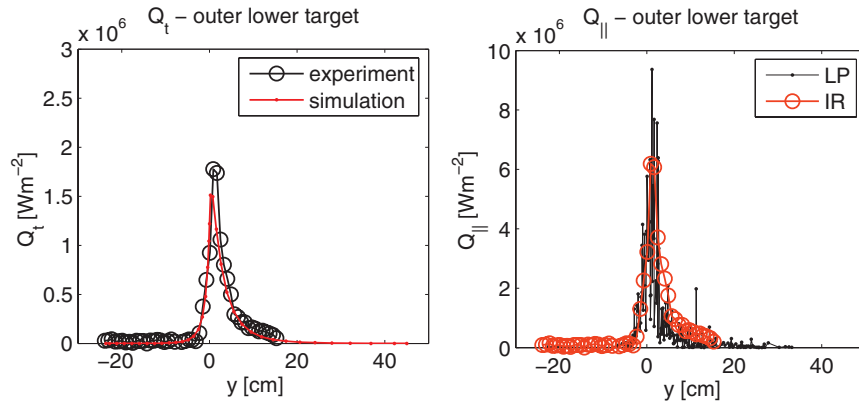


Figure 4. Comparison of the simulated energy flux density at the outer target deposited by electrons and ions and the one measured by IR (left), comparison of the energy flux density at the target measured by IR and LP (right) with the LP signal calculated as $Q_{||} = 7T_e n_e c_s$. Q_t is the energy flux density normal to the target, while $Q_{||}$ is the parallel energy flux density.

the modelling is consistent with recent multi-machine scalings [18] when the uncertainty in the regression is taken into account.

Also the simulated $D\alpha$ emissivity fits well the experimental measurement at the midplane (figure 5). A shift between the peak values of 1 cm supports the assumption that a shift of the equilibrium with respect to the experimental profiles of 1 cm can be allowed.

Finally, the molecular density in the simulation is compared with a measurement from the pressure gauge located in the main chamber at the midplane (figure 1). Since the density outside the plasma grid is not directly available in the simulation, we compare the experimental value of $1.3 \times 10^{18} \text{ m}^{-3}$ with the simulated value at the boundary of the grid of $1.6 \times 10^{18} \text{ m}^{-3}$ (see figure 6). Unfortunately, the data from a pressure gauge located in the divertor chamber are unavailable for comparison.

Good agreement between the experiment and modelling has been found for available diagnostics data including densities and temperatures in the scrape-off layer, energy fluxes to the target, $D\alpha$ radiation or molecular density at the midplane. This gives a basis to predict conditions in the MAST-U divertor in section 3.

3. Predictions for MAST Upgrade

3.1. Divertor geometry in MAST Upgrade

In comparison to MAST (figure 1), MAST-U will operate with a closed divertor and a system of cryopumps in both lower and upper divertor chambers (figure 7). As shown in figure 7, the divertor closure is managed by means of a baffle structure. Since the baffle significantly reduces the leakage into the main chamber, in the model we assume only the leakage through the divertor throat.

Apart from the closed design and increased pumping efficiency, conditions in the outer divertor can be influenced by the magnetic topology which can be optimized in order to reduce plasma temperatures and heat fluxes at the target plate. MAST-U is designed to explore the range of topologies with different strike point radius, connection length and

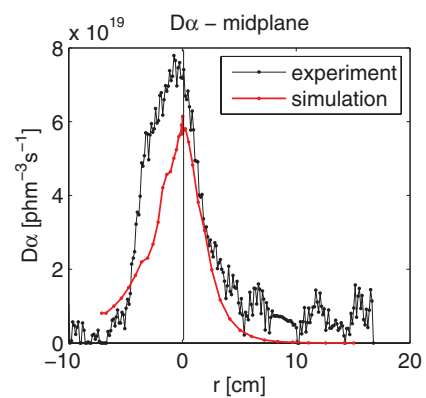


Figure 5. Comparison of the measured and simulated $D\alpha$ emissivity at the outer midplane.

flux expansion, allowing the Super-x and snowflake divertors. Three magnetic topologies considered in the simulation are shown in figures 7 and 8.

In figure 8 and table 1, the flux expansion in the divertor of MAST-U is also compared with the equilibrium obtained for the MAST shot 30356 described in the previous section. The separation into the poloidal magnetic flux expansion, the toroidal magnetic flux expansion and the flux expansion caused by the target tilting (table 1) shows that the total flux expansion in the CD is increased compared to MAST mainly due to the target tilting. In the SXD1, the flux expansion increases further due to larger radius of the target plate (larger toroidal flux expansion) and due to reduced poloidal field in the divertor (larger poloidal flux expansion). The SXD2 is an intermediate case between the CD and SXD1 with larger toroidal flux expansion, but smaller poloidal flux expansion.

In addition to the magnetic topologies CD, SXD1 and SXD2, we also consider a simulation of the SXD where the baffle is removed, assuming the magnetic topology of the SXD1. This case will be labelled as SXD3.

3.2. Low power case

Simulation parameters used for MAST-U are the same as in the simulation of the MAST discharge 30356 ($P_{\text{inp}} = 1.7$

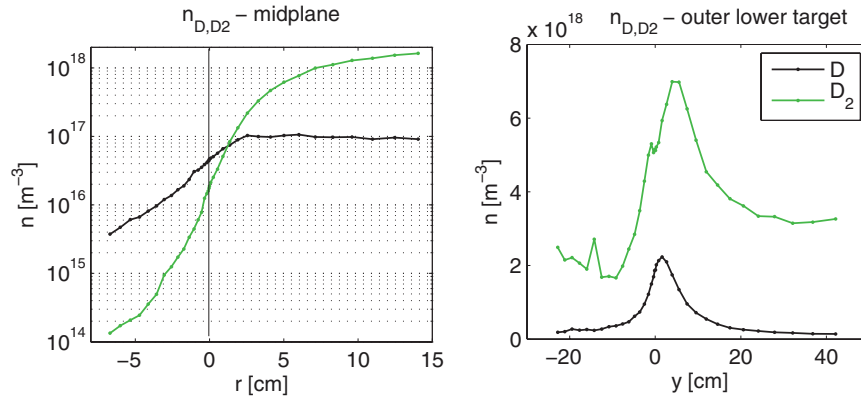


Figure 6. Radial profiles of the atomic and molecular density at the outer midplane (left) and at the outer target (right).

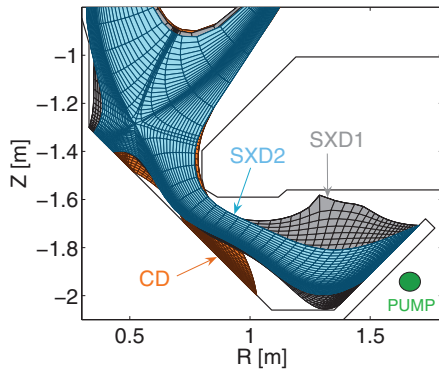


Figure 7. Magnetic geometry in the MAST-U divertor considered in the simulation: CD (orange), SXD1 (black), SXD2 (blue). The position of the cryopump is indicated.

MW, $n_{\text{core}} = 1.3 \times 10^{19} \text{ m}^{-3}$), only the magnetic topology is changed and the pumping efficiency is increased from $10.7 \text{ m}^3 \text{ s}^{-1}$ used in MAST to $42 \text{ m}^3 \text{ s}^{-1}$ in MAST-U to take into account larger pumping speed available in MAST-U. The code adjusts the ion flux across the core boundary in order to retain the core density as follows: $2.8 \times 10^{21} \text{ s}^{-1}$ (MAST), $7.7 \times 10^{21} \text{ s}^{-1}$ (CD), $8.3 \times 10^{21} \text{ s}^{-1}$ (SXD1), $8.5 \times 10^{21} \text{ s}^{-1}$ (SXD2) and $3.4 \times 10^{21} \text{ s}^{-1}$ (SXD3). Figure 9 shows simulated radial profiles of the density and temperature at the outer midplane and along the outer target. Plasma parameters in the inner SOL are not shown, as they are not affected by geometric changes in the outer divertor. For example the electron temperature at the inner target for simulations in figure 9 varies between 30 and 44 eV, which is correlated with the variation of the inner midplane temperature of 44–55 eV. Similar upstream densities and temperatures are obtained regardless of the divertor geometry also in the outer SOL, while conditions in the outer divertor change significantly and this can be ascribed to the combination of baffling and changes in the magnetic topology. Note that there is a small variation in values at the midplane (e.g. between CD and SXD1), which is caused by a tolerance in the prescribed core density set by the code. The smaller value of the ion temperature at the midplane for the SXD3 case (and MAST) and the higher value of the density is, however, due to the open divertor (neutrals escaping the divertor contribute to larger density as well as they cool the plasma in the upper SOL).

Table 1. Flux expansion factors in the outer SOL averaged over 1 cm of the radial distance at the midplane.

	$\langle \text{FX} \rangle$	$\langle \text{FX} \rangle_{\text{pol}}$	$\langle \text{FX} \rangle_{\text{tor}}$	$\langle \text{FX} \rangle_{\text{tilt}}$	$\langle dy/dr \rangle$
MAST	1.8	2.3	0.7	1.1	2.9
MAST-U CD	6.6	3.3	0.6	3.1	12.5
MAST-U SXD1	20.2	5.9	1.2	2.8	20.5
MAST-U SXD2	12.4	2.4	1.2	4.3	12.2

Note: $\langle \text{FX} \rangle$ is the total flux expansion, $\langle \text{FX} \rangle_{\text{pol}}$ and $\langle \text{FX} \rangle_{\text{tor}}$ is the poloidal and toroidal magnetic flux expansion, $\langle \text{FX} \rangle_{\text{tilt}}$ is the flux expansion caused by the target tilting, $\langle dy/dr \rangle$ is the expansion related to the projection from the radial midplane coordinate r to the target coordinate y . The total flux expansion can be approximately calculated as $\langle \text{FX} \rangle \approx \langle \text{FX} \rangle_{\text{pol}} \times \langle \text{FX} \rangle_{\text{tor}} \times \langle \text{FX} \rangle_{\text{tilt}}$ and the exact definitions are given in [7].

The electron temperature at the outer target drops to approximately 1 eV in MAST-U with the SXD, and similar divertor temperatures are achieved in the SXD1 (0.8 eV) and SXD2 (1.1 eV). This suggests that an additional poloidal flux expansion inside the SXD in MAST-U does not have a strong effect on the access to detachment (this has been already shown in [9] for an impurity seeded transition to detachment).

MAST-U with the CD is still attached with the target temperature of 20 eV. The difference between the CD and the shot 30356 (labelled as MAST) is perhaps not as large as one would expect from open versus closed divertor. This comes from a combination of larger divertor closure with respect to neutrals in the CD case (increasing the neutral pressure), but also stronger pumping in MAST-U (reducing the neutral pressure). The CD therefore achieves rather similar divertor parameters as MAST, but what changes dramatically is the ratio between the divertor and upstream atomic and molecular pressures.

Figure 9 also indicates that the amount of neutrals in the divertor is an important factor for the access to detachment, as the SXD without the baffle (labelled as SXD3), where neutrals are free to escape the divertor, is attached. The baffle causes a drop of the electron temperature at the target from 10 eV to 1 eV and an increase of the target density, proving a strong role of neutrals in reducing the divertor temperature and the detachment threshold. This could also explain the difficulties to make the outer divertor detach in current MAST discharges. Further, one can notice a large change in target conditions between the SXD3 and MAST. Since both divertors are

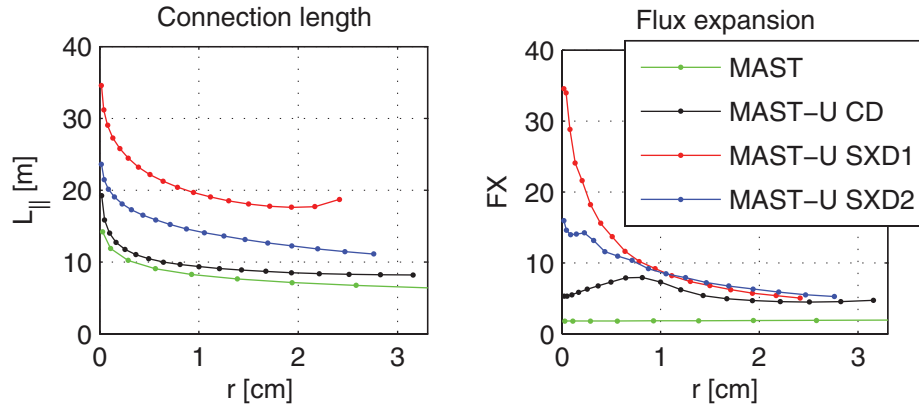


Figure 8. The midplane to target connection length (left) and the total flux expansion (right) in the outer SOL in MAST from figure 1 and MAST-U from figure 7.

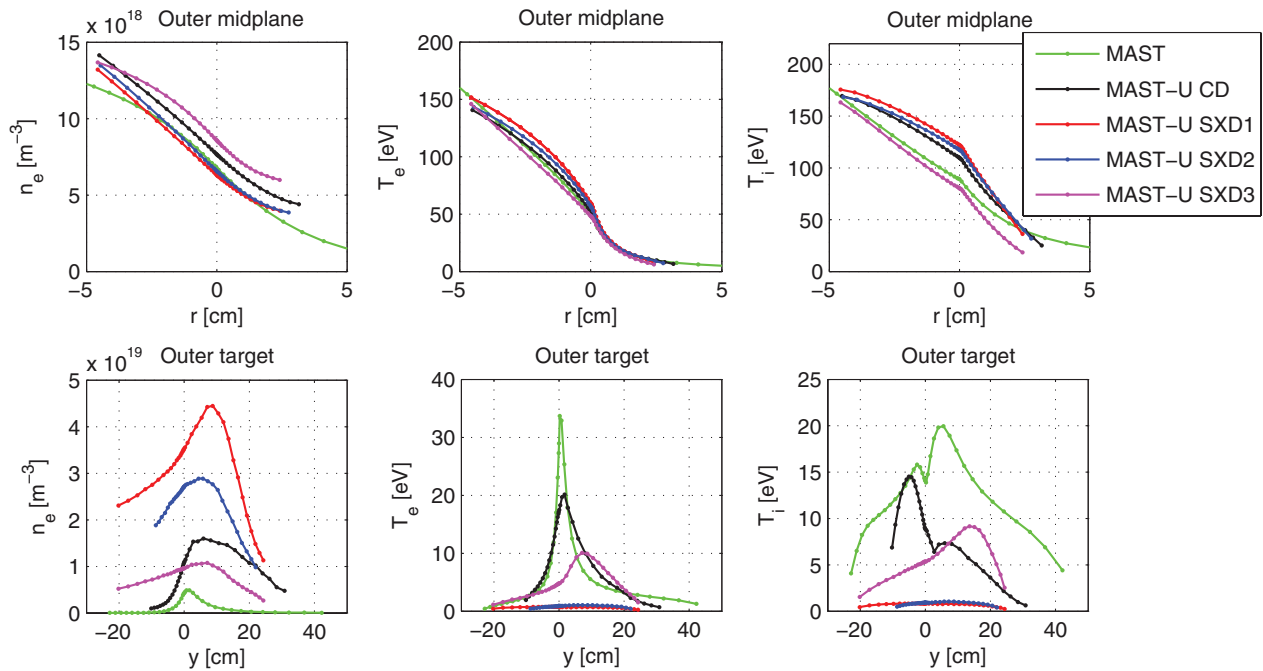


Figure 9. Radial profiles of the electron density (left), the electron temperature (middle) and the ion temperature (right) at the outer midplane (top) and at the outer target (bottom). The radial midplane coordinate r and the target coordinate y measure the distance from the separatrix which is represented by 0.

open and upstream conditions are similar, this change can be related to the change of the flux expansion (but combined with stronger pumping in MAST-U).

The SXD2 with low poloidal flux expansion differs only slightly from the flux-expanded one in terms of the divertor temperatures and the divertor closure with respect to neutral species, and the main effect of the additional poloidal flux expansion is in a reduction of the energy flux to the target (discussed later). The effect of the additional flux expansion, compared to the effect of larger target radius, depends on the collisionality regime. In detached cases with high power losses, the effect of the flux expansion is weaker than the effect of radiation and plasma-neutral interactions which set the conditions in the divertor. The importance of plasma-neutral interactions in MAST-U is due to its closed divertor design.

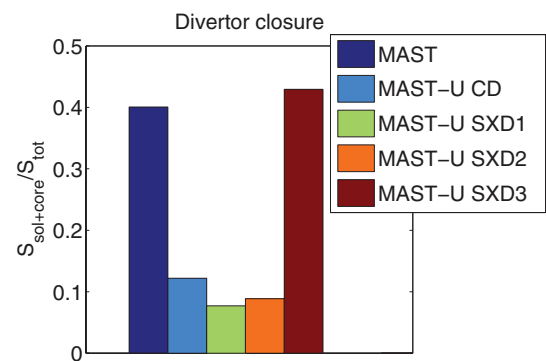


Figure 10. Divertor closure with respect to neutrals calculated as the ionization source in the simulation grid outside the divertor region with respect to the ionization source in the whole grid.

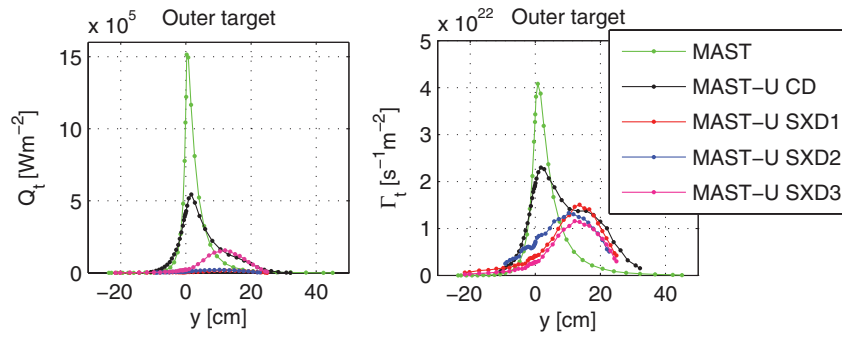


Figure 11. Radial profiles of the energy (left) and particle (right) flux densities at the outer target normal to the target surface. The energy flux density is calculated as $Q_t = 5/2k(T_e + T_i)\Gamma_t + 1/2m_iu_{||}^2\Gamma_t + q_e + q_i$ where $q_{e,i}$ is the conductive heat flux density.

The divertor closure is shown in figure 10 and is measured as the ratio of the ionization source outside the divertor (including the core and upper SOL part of the grid) and the total ionization source in the grid. The effect of the baffle in MAST-U is clearly visible (compare with MAST and SXD3). The baffle reduces the leakage of molecules and atoms from the divertor chamber and increases the neutral compression between the divertor and the midplane. As the result, the atomic and molecular densities in the core in MAST are larger than in the core in MAST-U by an order of magnitude, in spite of smaller densities in the divertor. The SXD1 and SXD2 configurations achieve similar level of the closure, while the closure in the CD is slightly weaker due to shorter distance between the target and the X-point and larger ionization mean free path (larger temperature and smaller density in the CD). Note also that in the CD, neutral densities in the divertor are smaller than in the SXD, but comparable at the X-point and in the core.

A reduction of the energy flux density at the outer target related to the modification of the divertor geometry is shown in figure 11 and is partly caused by the magnetic topology (see the flux expansion in table 1), but also by power losses due to radiation, ionization and charge exchange. The peak target energy flux density drops from 1.5 MWm^{-2} in the simulation of the shot 30356 to 0.5 MWm^{-2} in MAST-U with the CD (a factor of 3, equal to the effect of the flux expansion), and is further reduced to 17 kWm^{-2} in the SXD1 or similarly to 21 kWm^{-2} in the SXD2 (a factor of 25, due to the flux expansion and power losses). This large drop is caused by the transition to detachment and shows the importance of strong volumetric power losses in comparison to the effect of magnetic flux expansion.

Power balance in MAST and MAST-U combining attached (MAST, CD, SXD3) and detached cases (SXD1, SXD2) is presented in figure 12 with the power to solid surfaces shown in blue and the power loss shown in yellow (the power radiated by carbon ions), orange (the power radiated by neutral species—D, C, D₂) and red (the power loss caused by ionization and charge exchange). The graph shows a reduction of the power deposited at the outer target in MAST-U compared to MAST (dark blue), especially with the SXD, accompanied by an increase in the radiated power in MAST-U thanks to the increased flux expansion and the baffle (the larger the neutral pressure in the divertor, the more radiation and cooling). The

total power loss increases by nearly a factor of 2 in the SXD compared to the CD and is similar in the two SXD configurations. Strong neutral leakage from the SXD represented by the SXD3 case reduces the power loss by a factor of 1.5, to a similar level as the CD with the baffle. Thus it appears that the neutrals can have an effect on the divertor solution similar in strength to significant changes in R in going from the CD to SXD.

In figure 12, the MAST-U configurations receive less power to the outer targets, especially the SXD cases, but more power leaves the grid radially as P_{wall} and can be potentially deposited at the main chamber wall. Note that this is likely due to a narrower grid in MAST-U. The grid for plasma in SOLPS is limited by the flux surface which is in contact with the vessel wall (and the so-called leakage boundary condition is applied to the density and the decay lengths are prescribed for the temperatures [19]), while the domain for neutrals fills the whole vessel. Because the grid does not extend to the actual wall, we cannot directly determine the power reaching the wall and thus an accurate measure of P_{wall} . Instead, utilising a simple extrapolation technique, we made a maximum estimate of the power radiated outside the grid. We found that, if the radiation level does not decay between the grid boundary and the main chamber wall, the power radiated beyond the grid boundary can be substantial, potentially accounting for all the power leaving the grid. However, the uncertainties in this extrapolation are large. A simulation with a grid extending up to the wall would be required for a confident quantitative estimate.

Table 2 shows the radiated power (and also the total power loss, since not all the power loss is due to radiation) in different regions of the simulation grid. In MAST and the SXD3, the power loss above the X-points exceeds the power loss in the divertors, while the MAST-U cases with the baffle favour divertor power losses. The distribution of the radiated power in the divertor can be compared in figure 13. Total radiation is shown (left) as well as its components that are separated in the simulation as line radiation from carbon ions (middle) and radiation from neutral species (right). The radiation pattern shows an attached plasma in MAST and the CD and SXD3 of MAST-U with the peak radiation around the strike point, while the radiation in the SXD1 and SXD2 takes place inside the divertor leg. The SXD provides larger radiation volume than the CD (the radiation zone is extended in the SXD in the direction of the magnetic field), which is consistent with the

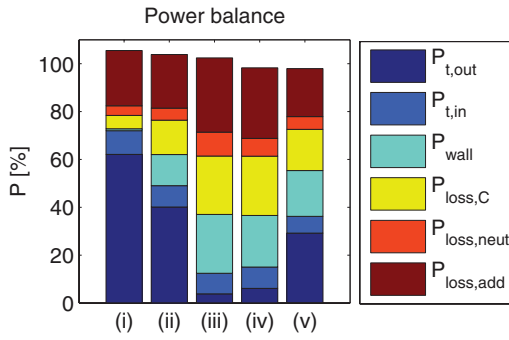


Figure 12. Power balance in the simulation of MAST (i), MAST-U with the CD (ii), MAST-U with the SXD1 (iii), MAST-U with the SXD2 (iv) and MAST-U with the SXD3 (v) with the input power $P_{inp} = 1.7$ MW. $P_{t,out}$ and $P_{t,in}$ is the power to the outer and inner target, P_{wall} is the power leaving the grid radially, $P_{loss,C}$ is the power radiated by carbon ions (line radiation), $P_{loss,neut}$ is the power radiated by neutral species (line radiation, three-body recombination, molecular dissociation), $P_{loss,add}$ is an additional power loss caused by plasma-neutral interaction (ionization, charge exchange). Note that due to the limited grid size in SOLPS, P_{wall} includes both the energy flux deposited by the plasma at solid surfaces and the power radiated outside the plasma grid. Therefore the increase in P_{wall} from MAST to MAST-U can be partly due to a narrower grid in the MAST-U cases. Also note that only the main power balance components are shown and that is why the components do not sum up to 100% exactly. The power to the targets is calculated by integration of the electron and ion energy flux (defined in the caption of figure 11) over the target surface and all ionic species and excludes the power from the ion viscous flux which is treated separately in the simulation as a viscous heating term. The viscous heating term, that would lower the power to the targets, reaches approximately 8% in MAST, 6% in the SXD3 and 4% in the CD, SXD1 and SXD2.

Table 2. The total power loss (the first number) and the radiated power (the second number) in MAST and MAST-U simulations in the core part of the grid (i), in the SOL above the X-point (ii), in the inner divertors (iii) and in the outer divertors (iv).

	Core	Upper SOL	Inner divertors	Outer divertors
MAST	9.5/1.9	8.6/1.7	2.1/1.2	12.5/4.9
MAST-U CD	3.1/2.2	5.0/2.9	2.1/1.5	31.8/12.9
MAST-U SXD1	2.7/1.4	3.1/1.6	1.3/1.0	58.2/30.5
MAST-U SXD2	2.7/1.7	3.3/1.7	1.7/1.1	54.0/27.6
MAST-U SXD3	9.6/3.9	12.1/4.9	1.3/1.0	19.6/12.7

increased radiated power in figure 12. Finally, one observes a radial broadening of the radiation zone with the poloidal flux expansion in the SXD1 compared to the SXD2. However, this broadening does not significantly change the total radiated power for the detached SXD cases (figures 12 and 13). The total power loss is increased only by a factor of 1.06 in the SXD2 with respect to the SXD1. In contrast, the change from an attached CD to a detached SXD corresponds to an increase in power losses by a factor of 1.6.

We have also analyzed the radiated power in the flux-expanded region in more detail. Figure 14 on the left shows the radiated power in the SXD1 and SXD2 integrated from the X-point towards the target as a function of the poloidal coordinate. Also shown are the radiation profiles across the divertor leg

at $R = 0.9$ m (middle) and $R = 1.3$ m (right). The data confirm a broadening of the radiation profile inside the flux-expanded region (right). The amplitude of the radiated power density is, however, smaller in the SXD1 towards the X-point at the end of the poloidal flux-expanded region (middle). While the integral of the radiation profile just inside the flux-expanded zone in figure 14 on the right increases by a non-negligible factor of 1.6 in the SXD1 compared to the SXD2, the power loss integrated across the whole flux-expanded region increases only by a factor of 1.13. The radiative losses are then clearly redistributed by poloidal flux expansion in the divertor, however, the overall effect on the power loss, at least in this case, is small.

Finally, while not shown explicitly here, we find that carbon radiation is more effectively confined inside the divertor region in the SXD configurations (SXD1 and SXD2) than in the CD. We draw this conclusion because the total radiation in the grid from impurities in the SXD cases is almost a factor of 2 larger than for the CD divertor, while radiation in the core part of the grid is lower for the SXD than for the CD.

3.3. High power case

There are several ways to reduce temperatures in the divertor and access a detached regime, for example increasing the gas puff density, reducing the heating power or puffing additional impurities [20, 21]. In MAST-U, the transition to detachment can be also induced by modifications of the divertor magnetic topology.

Based on the study of MAST-U at power levels of MAST, the SXD topology would appear to always lead to detachment at low heating power. Note that in this paper, we simply consider the plasma is detached if the peak target temperature is below 5 eV. We now address what the effect of higher power levels would be in the divertor configurations from figure 7. We also assume slightly increased density $n_{core} = 1.7 \times 10^{19} \text{ m}^{-3}$ due to higher current of 1 MA in the simulated MAST-U cases. Figure 15 shows that the SXD1 with $P_{inp} = 3.5$ MW is just around the detachment threshold with the peak electron temperature at the target $T_e \approx 4.5$ eV. This means that an attached regime can be obtained in the SXD if the heating power or the pumping speed is increased further assuming the density does not change (see power and pumping scans in the next section).

As a measure of a reduction of the detachment threshold in the SXD, we also examined how much the density has to be increased or the input power lowered in the CD from figure 15 to achieve target temperature of around 5 eV as in the SXD1 case. Based on SOLPS calculations, we found that the CD with 3.5 MW of the input power would allow the access to detachment at approximately 3 times higher separatrix density n_{sep} than the SXD1 (corresponding to 3–4 higher n_{core}). Similar result was obtained in [8] for a MAST-U case with narrow SOL. Alternatively, at the given density of $n_{core} \approx 1.7 \times 10^{19} \text{ m}^{-3}$ and $n_{sep} \approx 1 \times 10^{19} \text{ m}^{-3}$, the transition to detachment would occur in the CD at approximately 4 times lower input power. These factors are slightly higher than those calculated from the modified two-point model [4] that accounts for the effect of varying target radius and which gives a factor of 2.2

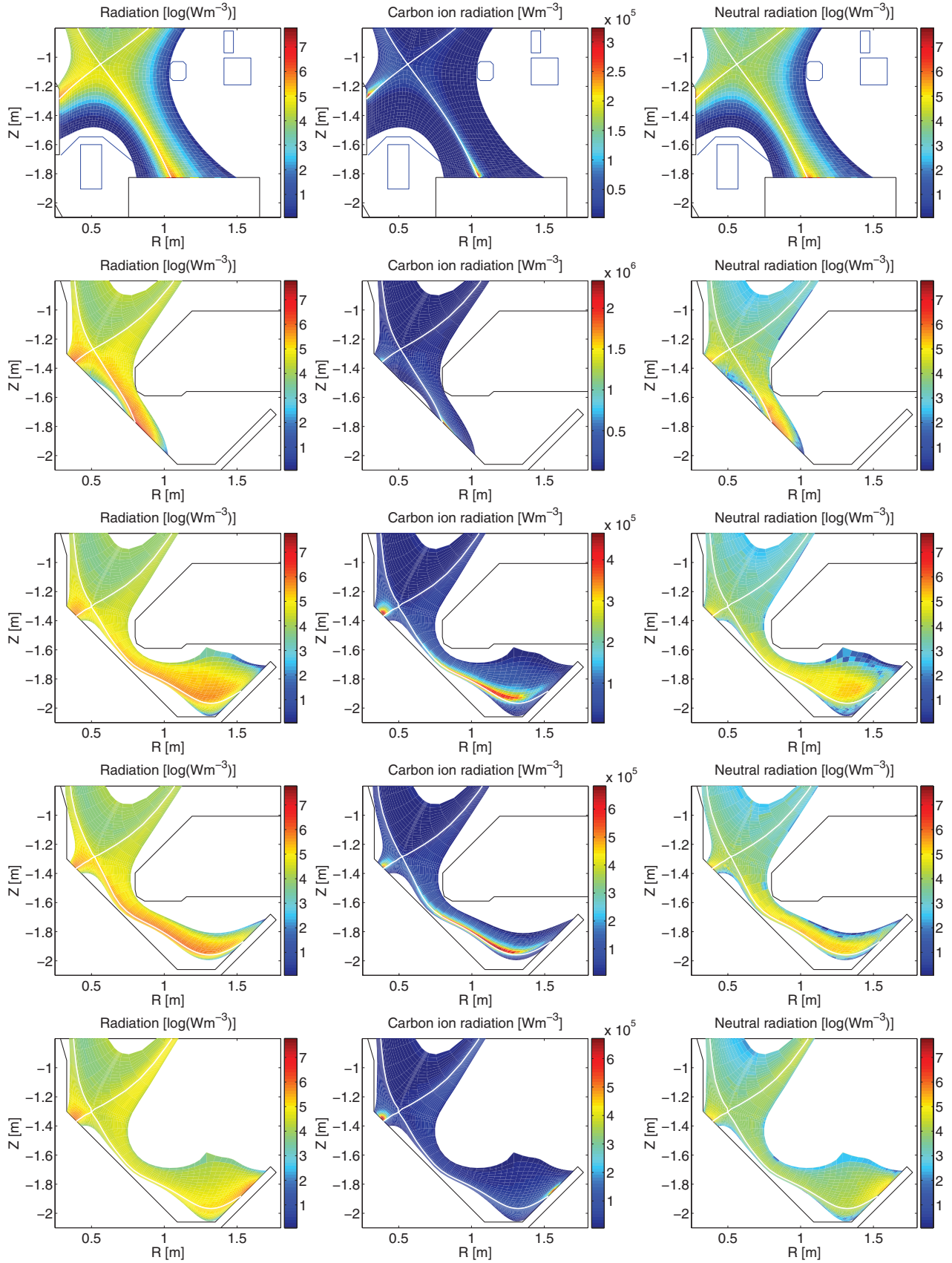


Figure 13. The distribution of the total radiation (left) and its components—the carbon ion line radiation (middle) and the radiation from neutral species (right)—in MAST (i), CD (ii), SXD1 (iii), SXD2 (iv), SXD3 (v).

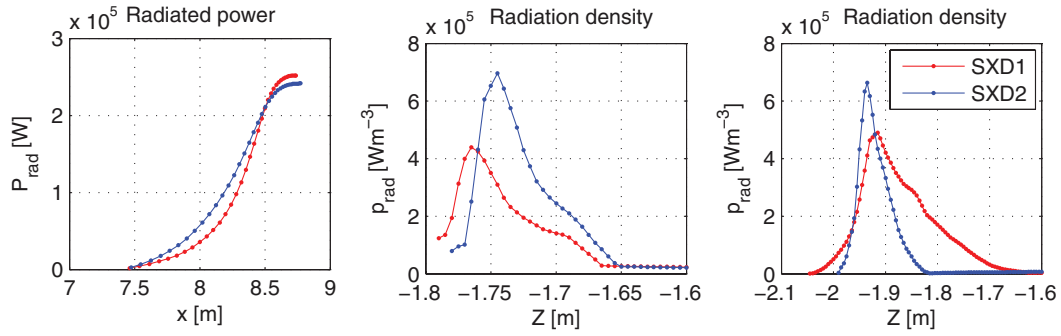


Figure 14. On the left, radiated power in the SXD1 and SXD2 as a function of the poloidal coordinate integrated between the X-point and the poloidal distance x . The coordinate x ranges from the X-point to the target. In the middle, a radiation profile taken vertically across the divertor at $R = 0.9$ m. On the right, a radiation profile taken vertically across the divertor at $R = 1.3$ m.

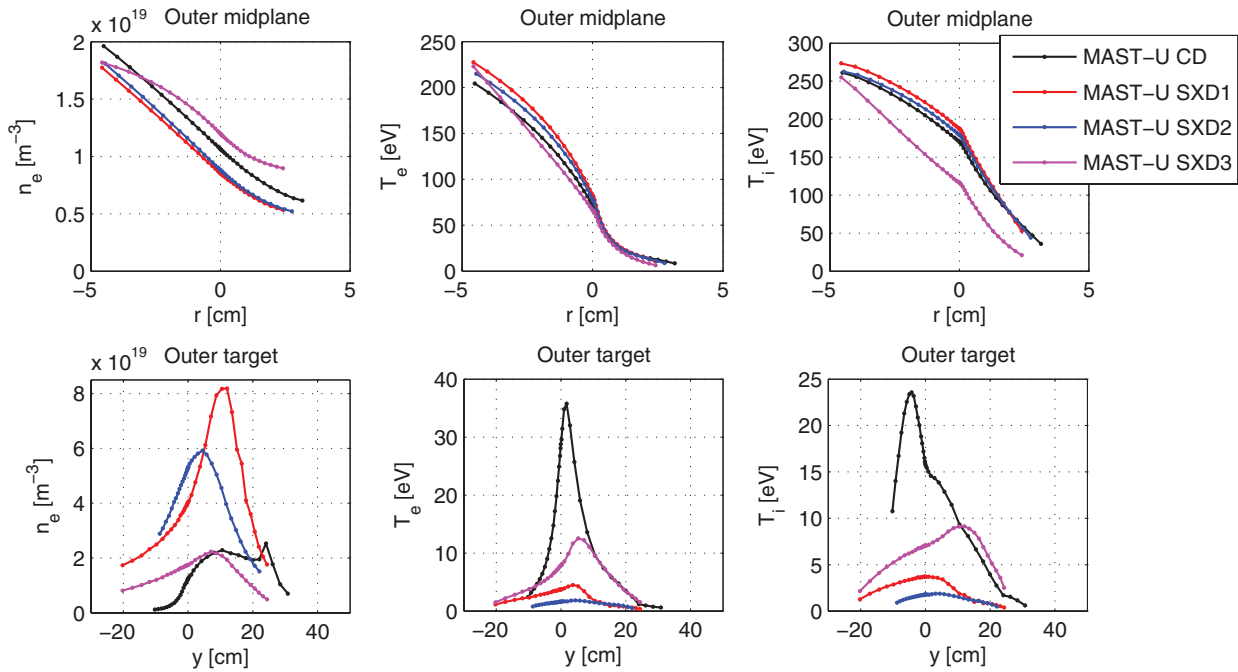


Figure 15. Radial profiles of the electron density (left), the electron temperature (middle) and the ion temperature (right) at the outer midplane (top) and at the outer target (bottom).

increase of the separatrix density and a factor of 3.1 reduction of the input power (assuming the connection length $L_{\parallel} \approx 20$ m in the CD and $L_{\parallel} \approx 35$ m in the SXD1, and the target radius $R_t \approx 0.8$ m in the CD and $R_t \approx 1.53$ m in the SXD1). Note that the target temperature in the two-point model is modified only as the result of geometry, taking into account the target radius and the connection length, while in SOLPS, both geometric effects and cooling due to plasma-neutral interactions are involved. In [9], the effect of the SXD topology on the detachment threshold in a nitrogen seeded plasma has been studied, resulting in a factor of 7 lower nitrogen seeding rate required for the outer leg to detach in the SXD compared to the CD.

4. Dependence of detachment on input power and pumping in the MAST-U Super-x divertor

As part of the study of the detachment threshold in MAST-U, we examined the effect of varying the amount of input power and cryopumping on the SXD case (SXD1) only.

Figure 16 presents the results of an input power scan where the divertor temperature (figure 16 right) is varied due to increases in the upstream temperature (figure 16 left). The density is not influenced by increasing power. Figure 16 shows that attached conditions can be achieved in the SXD at higher power levels, for this particular L-mode case for the input power above 3.5 MW. The maximum heating power available in MAST-U at later stages will be 12 MW, but not all the power is used due to losses. In MAST, the power crossing the separatrix as the input power P_{inp} is typically one to two thirds of the heating power.

An increase of the pumping speed on cryopumps (figure 17) modifies both target density (figure 17 left) and temperature (figure 17 right), while the upstream values are affected only slightly. The MAST-U design value for the cryopump is $50\text{--}60 \text{ m}^3 \text{ s}^{-1}$ which increases the divertor temperature over the level of pumping used in this study (figure 17).

Note that the effect of the density and the SOL width is not investigated in this study, where conditions in the divertor

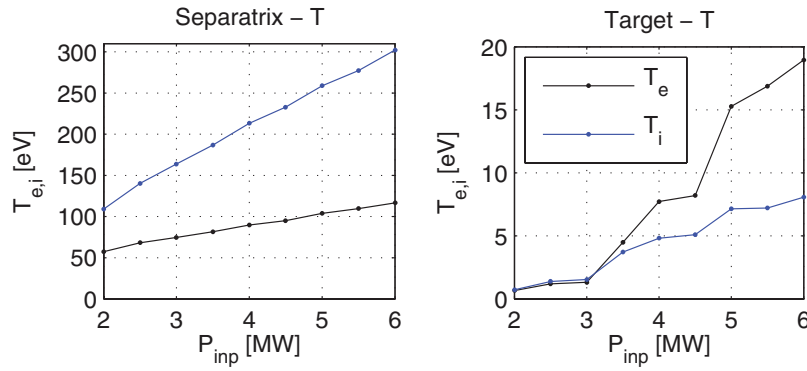


Figure 16. The upstream (left) and the peak target (right) electron and ion temperatures in the outer SOL as functions of the input power in the simulation of the SXD1 with the pumping speed of $42 \text{ m}^3 \text{ s}^{-1}$. In the inner SOL, the upstream T_e ranges between 53 and 110 eV and T_i between 97 and 270 eV (as at the outer midplane), and the inner targets are attached with T_e between 40 and 97 eV and T_i between 23 and 86 eV. The upstream and target densities are approximately $0.8 \times 10^{19} \text{ m}^{-3}$.

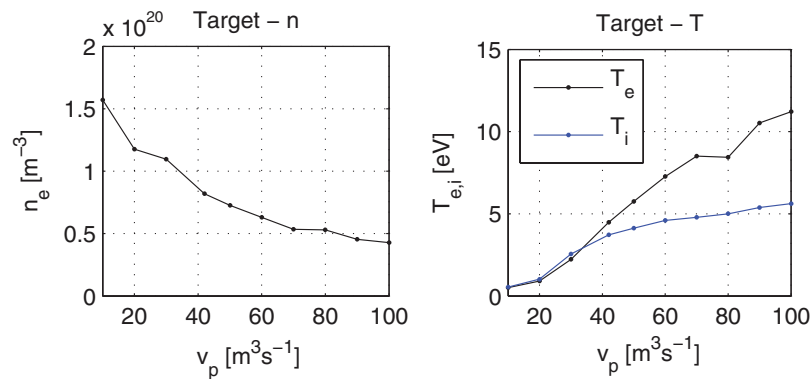


Figure 17. The peak target electron density (left) and the peak target electron and ion temperatures (right) in the outer SOL as functions of the pumping speed in the simulation of the SXD1 with the input power of 3.5 MW. The upstream density changes from 0.9 to $0.8 \times 10^{19} \text{ m}^{-3}$, and the upstream temperature increases from 76 to 86 eV for electrons and from 176 to 193 for ions. In the inner SOL, values at the midplane are: 0.8 to $0.7 \times 10^{19} \text{ m}^{-3}$ for the density, 70–80 eV for T_e , 153–172 for T_i , and values at the inner target are: 1.2 – $0.7 \times 10^{19} \text{ m}^{-3}$ for the density, 52–69 eV for T_e , 32–53 for T_i .

are parametrized using P_{inp} and v_p at fixed density and radial transport. We also speculate, that the operational space in attached plasmas would be broader in H-mode due to typically narrower SOL, see [17, 22], which would lead to larger upstream and peak target temperatures, if the power crossing the separatrix remains the same. Re-attachment during ELMs is another possibility to study the transition from attached to detached conditions. Alternatively, the attachment window would be extended during time-dependent passive pumping in the discharge before reaching a steady-state phase studied.

5. Conclusions

A SOLPS simulation of the MAST L-mode discharge 30356 has been successfully benchmarked against experimentally measured data. A good agreement has been achieved between the code results and all available diagnostics including Thomson scattering profiles, Langmuir probes divertor profiles, $D\alpha$ measurement, infrared camera data and molecular density measurement. This comparison is used to obtain a set of radial transport coefficients representative of MAST L-mode plasmas, which gives a good basis to predict conditions in the MAST-U divertor, again for L-mode conditions.

Both the conventional and Super-x double-null topologies are investigated for MAST-U.

Modelling results show that the MAST-U divertor exhibits dramatically better closure with respect to neutral species compared to the open MAST divertor, thanks to baffling, and achieves larger power losses and a reduction of the target power load. The divertor operational regime can be further influenced by a modification of the divertor magnetic geometry. In MAST-U, the SXD magnetic geometry can be obtained in the outer divertor, which affects the outer divertor conditions, but does not affect conditions in the inner divertor thanks to the double-null topology. The power load to the target is significantly reduced in the SXD (a factor of 25) compared to the CD as the result of plasma detachment. The radiation zone expands in the SXD compared to the CD and the total radiated power nearly doubles. In the studied case of a low power detached SXD L-mode plasma, addition of poloidal flux expansion leads to an increase in power losses small compared to changes in topology studied (e.g. CD to SXD). This could be because either the flux expansion just re-arranges the existing radiation or that in detached regimes the radiation integrated along each flux tube saturates at a level approaching the parallel heat flux further upstream. Since the additional poloidal flux expansion does not strongly

modify the target temperature for the SXD case studied, we speculate that it might also not influence the access to detachment. However, the effect of poloidal flux expansion on the detachment threshold requires further studies where the same attached condition is achieved for SXD and CD topologies.

Simulations based on the comparison of SOLPS with an L-mode MAST discharge predict detached divertor operation in the SXD of MAST-U, while the CD configuration with a shorter outer leg and smaller target major radius achieves rather similar divertor conditions as MAST. The addition of neutral leakage from the divertor has a strong effect on the access to detachment, such that the SXD divertor without the baffle would be attached. In L-mode, an attached plasma can be obtained in the SXD with the baffle as well, utilising levels of heating power and pumping efficiencies planned for MAST-U. Note that these predictions are based on a single comparison between the code and experiment for a typical L-mode case and are carried out assuming steady-state conditions. We expect that in H-mode with narrower SOL, higher peak target temperatures for the same power crossing the separatrix, as well as transients, would make SXD attached divertor operation available at lower input power and/or lower cryopumping speed. Finally, the simulation of MAST-U in L-mode shows that the SXD configuration lowers the detachment threshold by approximately a factor of 3 in the density and a factor of 4 in the input power compared to the CD configuration.

While atomic processes treated in the code included elastic collisions and molecular assisted processes relevant for detachment studies, neutral–neutral collisions and drift effects were not taken into account. Neutral–neutral collisions are not expected to have a significant effect here, as neutral densities in the studied MAST-U cases are below $1 \times 10^{20} \text{ m}^{-3}$. The effect of drifts has been studied for MAST in [23]. Important is the poloidal $E \times B$ drift which could result in asymmetries between upper and lower divertors and therefore influence the divertor detachment. In [23], drifts cause a change of 0–50% in the electron temperature at the outer targets.

Acknowledgments

This project has received funding from the European Union's Horizon 2020 research and innovation programme under grant agreement number 633053, from the RCUK Energy Programme [grant number EP/I501045] and from the Wolfson Research Fellowship. The views and opinions expressed herein do not necessarily reflect those of the European Commission. The author gratefully acknowledges the support of X Bonnin and D Coster.

Appendix A

A.1. Sensitivity of results to simulation parameters

Some of the previous simulations of MAST-U [7] and MAST discharges resulted in large temperatures in the SOL compared

to values typically observed in MAST experimentally. This motivates us to examine the sensitivity of modelling results for the discharge 30356 to simulation parameters which are unknown from experiment.

Among these are flux limiters, free model parameters used in fluid codes, for which no systematic study exists and their choice is to a certain extent intuitive. The SOLPS simulation of the discharge 30356 does not show a strong effect of the electron heat flux limiter (figure A1). This is due to small parallel temperature gradients. Moreover, the electron heat flux limiter is not required in middle to high collisionalities [24]. The ion heat flux limiter, on the contrary, has a large effect, therefore its value is important for comparing simulation results with ion temperature measurements. The viscous flux with stronger limiting $\beta = 0.1$ (figure A2) is not much different from the reference value of 0.5 and values below 0.1 are unlikely [24]. Weaker limiting with $\beta = 2.0$ increases the target temperature and reduces the target density by 20–30%. A comparison between kinetic and fluid models shows the values 0.5 or lower are appropriate for cases without recycling (sheath-limited), while larger values could be appropriate for high-recycling cases [24].

The effect of the sputtering yield coefficient was also tested. The simulation shows that the increase of the sputtering yield from 1 to 5% reduces the target temperature only by approximately 20%.

We also tested if the divertor temperature can be affected by lowering the pumping speed. It appears that the pumping speed in MAST is already low and its further reduction by a factor of 10 does not reduce the divertor temperature.

None of the parameters above allow a significant reduction of the electron temperature. Previously reported discrepancies could be therefore due to large input power assumed in simulations (the power crossing the separatrix in MAST is often much smaller than the heating power). Second, an experimental uncertainty in the separatrix position could allow the temperature to be lowered, especially in H-mode with steep gradients around the separatrix.

A.2. Comments on the separatrix position

As a rough guide for the separatrix position, T_e at the separatrix can be estimated from a simple analytic model [25], in the case of the discharge 30356 as $T_e \approx (7P_{\text{inp}}L_{\parallel}B/8\kappa_0\pi R\lambda_0B_{\text{pol}})^{2/7} \approx 40$ eV, or 32 eV if a uniform source is assumed instead of a localized one. This would suggest an outward shift of the TS profiles in figures 2 and 3, as the original experimental data show an average value around 25 eV. Such shift is consistent also with figure 5.

Alternatively, the two-point model [25] is often used to estimate the separatrix location. However, using the simple pressure balance as described by the two-point model appears to be inaccurate in our case according to the SOLPS simulation where more general equations than those defined by the two-point model are used (including loss terms and real geometry with $\nabla B \neq 0$). The simulation result shows that $2n_e^t/n_e^u T_e^t \neq 1$ (t denotes target values and u upstream values), see figure A3.

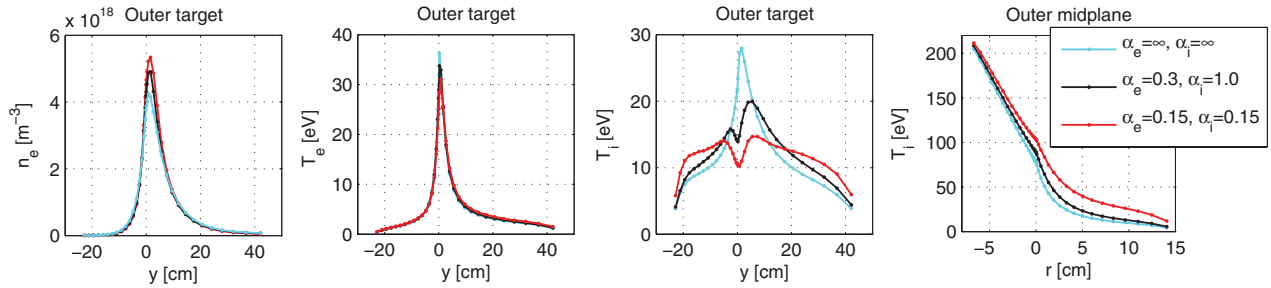


Figure A1. Radial profiles of the density and temperature at the outer target and midplane in the simulation with different heat flux limiters.

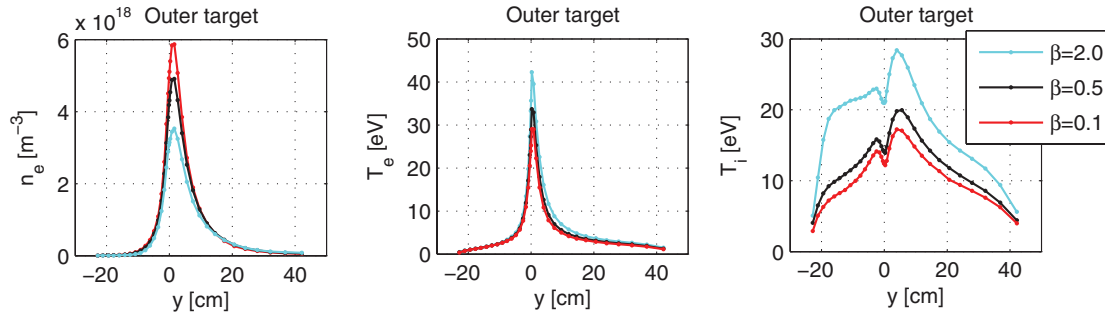


Figure A2. Radial profiles of the density and temperature at the outer target in the simulation with different viscous flux limiters.

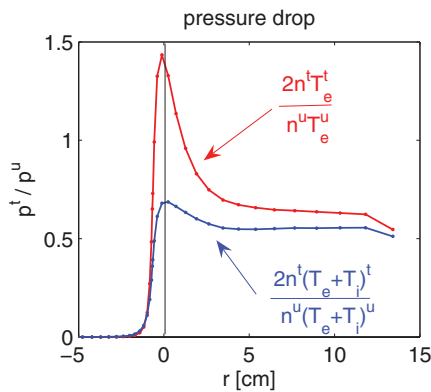


Figure A3. The ratio of the target and upstream pressure in the simulation calculated from expressions shown in the graph—(i) assuming $T_i = T_e$, (ii) allowing $T_i \neq T_e$.

Also notice a large change in the target/upstream pressure ratio p_t/p_u when the ion temperature is taken into account, as a result of $T_i > T_e$ in the simulation.

References

- [1] Morris W et al 2014 *IEEE Trans. Plasma Sci.* **42** 402
- [2] Fishpool G et al 2013 *J. Nucl. Mater.* **438** S356
- [3] Kotschenreuther M et al 2010 *Nucl. Fusion* **50** 035003
- [4] Stangeby P C *Modified Two Point Model of the SOL to allow for variation in R_{target}* http://starfire.utas.utoronto.ca/divimp/publications/2PM-with-R_t-variation-10Aug11-inc.pdf
- [5] Valanju P M et al 2009 *Phys. Plasmas* **16** 056110
- [6] Schneider R et al 2006 *Contrib. Plasma Phys.* **46** 3
- [7] Havlíčková E et al 2014 *Plasma Phys. Control. Fusion* **56** 075008
- [8] Havlíčková E et al 2014 *Contrib. Plasma Phys.* **54** 448
- [9] Havlíčková E et al *J. Nucl. Mater.* **463** 1209
- [10] Havlíčková E et al 2014 *21st Int. Conf. on Plasma Surface Interactions (Kanazawa, Japan)* p P2-045 to be submitted to PPCF
- [11] Reimold F et al 2014 *21st Int. Conf. on Plasma Surface Interactions (Kanazawa, Japan)* p I17
- [12] Aho-Mantila L et al 2012 *Nucl. Fusion* **52** 103006
- [13] Huang J et al 2010 *Plasma Phys. Control. Fusion* **52** 075012
- [14] Kirk A et al 2004 *Plasma Phys. Control. Fusion* **46** 1591
- [15] Field A R et al 2014 *Plasma Phys. Control. Fusion* **56** 025012
- [16] Hermann A et al 1995 *Plasma Phys. Control. Fusion* **37** 17
- [17] Harrison J et al 2013 *J. Nucl. Mater.* **438** S375
- [18] Scarabosio A et al 2013 *J. Nucl. Mater.* **438** S426
- [19] SOLPS manual <http://solps-mdsplus.aug.ipp.mpg.de:8080/solps/Documentation/solps.pdf>
- [20] Pitcher C S et al 1997 *J. Nucl. Mater.* **241–3** 696
- [21] Lipschultz B et al 1997 *J. Nucl. Mater.* **241–3** 771
- [22] Thornton A et al 2014 *Plasma Phys. Control. Fusion* **56** 055008
- [23] Rozhansky V et al 2012 *Nucl. Fusion* **52** 103017
- [24] Tskhakaya D 2014 private communications
- [25] Stangeby P C 2000 *The Plasma Boundary of Magnetic Fusion Devices* (Bristol: IOP Publishing)